Title	Localisation of normal faults in multilayer sequences
Author(s)	Schöpfer, Martin P. J.; Childs, Conrad; Walsh, John J.
Publication Date	2006-05
Publication information	Journal of Structural Geology, 28 (5): 816-833
Publisher	Elsevier
Link to publisher's version	http://dx.doi.org/10.1016/j.jsg.2006.02.003
This item's record/more information	http://hdl.handle.net/10197/3025
Rights	This is the author's version of a work that was accepted for publication in Journal of Structural Geology. Changes resulting from the publishing process, such as peer review, editing, corrections, structural formatting, and other quality control mechanisms may not be reflected in this document. Changes may have been made to this work since it was submitted for publication. A definitive version was subsequently published in Journal of Structural Geology Volume 28, Issue 5, May 2006, Pages 816-833 DOI#:10.1016/j.jsg.2006.02.003.
DOI	http://dx.doi.org/10.1016/j.jsg.2006.02.003

Localisation of normal faults in multilayer sequences

Martin P.J. Schöpfer*, Conrad Childs, John J. Walsh

Fault Analysis Group, School of Geological Sciences, University College Dublin, Belfield, Dublin 4, Ireland.

Abstract

Existing conceptual growth models for faults in layered sequences suggest that faults first localise in strong, and brittle, layers and are later linked in weak, and ductile, layers. We use the Discrete Element Method (DEM) for modelling the growth of a normal fault in a brittle/ductile multilayer sequence. The modelling reveals that faults in brittle/ductile sequences at low confining pressure and high strength contrast localise first as Mode I fractures in the brittle layers. Low amplitude monoclinal folding prior to failure is accommodated by ductile flow in the weak layers. The initially vertically segmented fault arrays are later linked via shallow dipping faults in the weak layers. Faults localise, therefore, as geometrically and kinematically coherent arrays of fault segments in which abandoned fault tips or splays are a product of the strain localisation process and do not necessarily indicate linkage of initially isolated faults. The modelling suggests that fault tip lines in layered sequences are more advanced in the strong layers compared to weak layers, where the difference in propagation distance is most likely related to strength and/or ductility

* Corresponding author.

Email: martin@fag.ucd.ie (MPJS) or fault@fag.ucd.ie (FAG)

contrast. Layer dependent variations in fault propagation rates generate fringed rather than smooth fault tip lines in multilayers.

Keywords: Discrete Element Method; fault growth; fault refraction; fault tip line; Mohr circles; stress and strain paths;

1 Introduction

There are a variety of conceptual models for the growth of faults in mechanically layered (brittle/ductile) sequences, all of which acknowledge that faults commonly show lithologically controlled dip changes on cross-sections, with steeper fault dips in strong layers and shallower dips in weaker layers (Fig. 1). These dip changes are attributed to a variety of mechanisms (Ferrill and Morris, 2003 and references therein): (i) post-faulting differential compaction, (ii) active faulting, with slip along layers or intersecting faults, (iii) linkage of an originally vertically-segmented fault and (iv) fault initiation with dip controlled by rock properties and effective stresses. Two of these mechanisms (iii and iv), which are not mutually exclusive, underpin the most popular models for the growth of faults within layered sequences. For mechanism (iii) faults first localise in the strong layers and are later linked via faults in the weak layers (Peacock and Sanderson, 1992; Eisenstadt and De Paor, 1987; Childs et al., 1996; Crider and Peacock, 2004). In this case, fault localisation and dips within the strong layers are controlled by rock properties and deformation conditions, and therefore by the failure mode and/or failure angles, while dips within the weak layers are a consequence of segment linkage. An alternative model (iv) suggests that localisation and associated dip changes do not develop in association with fault segmentation and are entirely controlled by the failure mode and failure angles of the faulted weak and strong layers. Distinguishing between these models on observational or theoretical grounds is not, however, always straightforward.

Ferrill and Morris (2003) describe small-scale faults exhibiting lithologically controlled dip variations. These authors consider two mechanisms of formation for the fault geometries they observe, these are, fault localisation first occurs within the strong layers (Fig. 2b) and fault localisation first occurs within the weak layers (Fig.

54 2c). In both cases fault dips are determined by the rheological properties of the layers
55 with steep dips in the strong layers and relatively shallow dips in the weak layers. The
56 faults studied by Ferrill and Morris (2003) do not have geometrical features which
57 might indicate whether they initiated in the strong or weak layers, e.g. abandoned tips
58 or splays. Other workers have described faults with lithologically controlled dip
59 variations which, from field relations, can be demonstrated to have formed by linkage
60 of segments which formed within the strong layers (e.g. Peacock and Zhang, 1993,
61 Childs et al., 1996). The absence of discriminating traits of segmentation, may support
62 the application of a model in which the faults were not, in fact, segmented in their
63 early stages of growth, but formed by refraction across bedding planes during
64 progressive forward tip-line propagation (Fig. 2d).
65 Although both linkage and forward propagation models (Fig. 2) provide a
66 plausible rationale for field observations that can be related to failure criteria, they
67 otherwise lack a mechanical basis. Mechanical analyses using failure criteria (e.g.
68 Coulomb-Mohr, Griffith) can provide useful insights into the orientation of principal
69 stresses and consequently faults, but do not allow definition of the relative timing of
70 failure and localisation in a mechanical multilayer (Mandl, 2000).
71 Since observational data and theoretical grounds do not provide a definitive
72 answer to questions relating to the localisation of faults within multilayers, we use a
73 numerical modelling approach which is capable of localising faults within multilayer
74 sequences. The aim of this paper is to provide a mechanical basis for the localisation
75 and linkage of normal faults in a layered sequence using the Discrete Element Method
76 (DEM). DEM has recently been used for modelling the formation of accretionary
77 wedges (Burbidge and Braun, 2002), fault-propagation folds (Finch et al., 2003 and
78 2004), out-of-plane fault propagation (Strayer and Suppe, 2003) and the interaction of

two overlapping faults (Imber et al., 2004). The method is capable of modelling failure and localisation without the necessity to define constitutive equations, as is the case for the more commonly used continuum methods. It is therefore the ideal tool for addressing questions relating to fault localisation in multilayered brittle/ductile sequences. As is described later, our models comprise brittle materials that deform by elastic deformation followed by fracturing and ultimately failure at peak strength, whilst our ductile material is frictional-plastic throughout deformation, displaying an inelastic deformation response without fracturing; these materials lead to macroscopic deformations that are discontinuous and continuous respectively. The results of the modelling support the notion that vertically segmented fault arrays initially develop in the strong, and brittle, layers and are later linked by shallower dipping faults in the weak, and ductile, layers.

2 Methods

2.1 *Principles of DEM*

The Discrete Element Method is a broad class of methods for modelling the finite displacements and rotations of discrete bodies (Cundall and Hart, 1992). DEM can be implemented in two and three dimensions. We use a 2D approach with circular particles as introduced by Cundall and Strack (1979) and implemented in commercially available software (*PFC-2D*, Itasca Consulting Group, 1999). Particles are treated as rigid discs and are allowed to overlap at particle-particle and particle-wall contacts. Walls are rigid boundaries of arbitrary shape, to which constant velocity or constant stress conditions can be applied. The amount of overlap at each contact is small compared to particle size and the contact normal force is linearly related to the amount of overlap. If the contact shear force exceeds a critical value,

which is determined by a contact friction coefficient, slip occurs at the contact. Particles can be bonded together with linear elastic cement (parallel bond model, Itasca Consulting Group, 1999; Potyondy and Cundall, 2004) and if the critical tensile or shear stress (which is typically normally distributed in a bonded model) at a bonded contact is exceeded the bond breaks.

For a more detailed description of this numerical method the reader is referred to Cundall and Hart (1992), Hazzard et al. (2000), Potyondy and Cundall (2004) and references therein.

2.2 *Model material calibration*

In contrast with continuum methods, where the rheology of the model material is defined using constitutive laws, the macroscopic response of the (bonded) particle assemblage in DEM models has to be calibrated using a numerical laboratory. The microproperties (particle size and size distribution, particle and bond stiffness, contact friction, bond strength) are adjusted, mainly by trial and error, to obtain the desired model macroscopic response calibrated to laboratory rock deformation data. The resulting microproperties do not replicate true grain-scale physics because the model particles are orders of magnitude larger than the grains of the equivalent rock and each particle therefore represents a small volume of rock. Although our approach did not attempt to exactly reproduce the rheology of a particular rock based on experimental data, the macroscopic properties of our model materials reproduce the general rheological behaviour of a strong, brittle material and a weak, ductile one.

The particles in this study have a uniform size distribution with r_{max} and r_{min} of 62.50mm and 31.25mm, respectively. The rheology of a strong material, consisting of bonded particles, and a weak material, consisting of non-bonded particles, was

investigated. The bonded particles have normal and shear contact/bond stiffnesses of 50GPa and 16.7GPa, respectively, a contact friction coefficient of 1.0 and normally distributed tensile and shear bond strengths with a mean of 250MPa and 125MPa and coefficients of variation of 1/12 and 1/6, respectively. The bond strength distributions have cut-offs of plus/minus two standard deviations and the width of each bond is half the radius of the smaller of the two bonded particles. The non-bonded particles have the same particle size and size distribution as the bonded material, a normal and shear contact stiffness of 50GPa and 16.7GPa, respectively, and a contact friction coefficient of 0.5.

The strength of bonded materials is sample size dependent (strength decreases with increasing sample size; Potyondy and Cundall, 2004), thus proper calibration requires tests on samples at a scale appropriate to the model. In our multilayer modelling, the basic mechanical unit is one bed. Therefore the rheology of both the bonded and non-bonded material was investigated using calibration sample widths equal to the thickness of the strong layers in the multilayer, i.e. 1m (see below).

The rheology of the non-bonded material was investigated using confined (25MPa) biaxial compression tests on samples that are 1m wide and 2m high. Since the material is cohesionless and exhibits no (bulk) elasticity the only bulk property that was calculated for each test (N = 30) is the friction coefficient, which can be easily obtained for straight failure envelopes.

The rheology of the bonded material was investigated using unconfined biaxial compression tests on samples that are 1m wide and 2m high. These tests (N = 30) were used for calculating the bulk elastic properties (Young's modulus, Poisson's ratio) and provided the unconfined compressive strength. Additionally direct tension

tests on dog-bone shaped samples (N = 196) with a central thickness of 1m were performed at various confining pressures in order to define the failure envelope in the tensile stress field.

Although calibration tests on 1m wide samples provide the bulk rheological properties and their variability at the scale of the multilayer model, they do not give insights into strain distribution (e.g. localisation) within the sample due to their poor resolution (*ca* 10 particles wide). To examine localisation behaviour in our model materials nine biaxial tests were performed on samples that are 5m wide and 10m high and contain over 6000 particles.

2.3 *Multilayer faulting model boundary conditions*

The multilayer model used is 15m wide, 13m high and is comprised of >23,400 particles (Fig. 3a). The model is composed of four 1m thick strong (bonded particles) and four 1.5m thick weak (non-bonded particles) layers. The top 3m of the model comprises a layer of non-bonded particles. The primary function of this top layer is model confinement, which is achieved by applying a force equivalent to a lithostatic stress of approximately 23MPa (*ca* 1km burial depth) to particles at the surface of the model. The sides and base of the model are defined by two rigid L-shaped walls which meet at a predefined 60º dipping fault at the base of the model. The L-shaped hanging wall is moved with constant velocity parallel to the predefined fault; this pre-conditioning ensures the formation of one fault, rather than several faults. The model is saved in 1cm throw increments and the final throw is 10cm; models with throws beyond the point of localisation (*ca* 10cm) will be published elsewhere. With respect to the ideal elliptical fault surface shown in Fig. 3b, the model is located in the plane of no lateral propagation along a chord through the point of maximum displacement.

2.4 *Stress and strain in discontinua*

Stress and strain are continuum concepts, whereas our model material is comprised of discrete particles and is therefore a discontinuum (compressive stress positive and $\sigma_I > \sigma_{II} > \sigma_{III}$). Various methods for homogenising DEM models to allow comparison with continuum mechanics solutions have been proposed and successfully implemented (e.g. O'Sullivan et al., 2003). The stress tensor can be obtained for each particle in our models, but the state of stress at this point is meaningless on a macroscale, i.e. on the scale of the layers. To homogenise particle stresses the average stress tensor is calculated for circular regions (Potyondy and Cundall, 2004).

The deformation tensor **D**, which is sometimes called the positions gradient tensor (see Appendix A), can be obtained for small and large strains using the least-squares method described in Oda and Iwashita (2000). For each circular region (diameter depends on the scale of interest) the particle closest to the centre is found and the relative displacements of particles surrounding this particle are calculated in order to remove the translational component of deformation. Once this translation has been removed the best-fit displacement gradient tensor can be calculated, enabling the deformation tensor **D** and the Lagrangian strain tensor **E** to be obtained.

For the maximum shear strain contour diagrams shown (e.g. Fig. 4e and f, Fig. 6) the diameter of the circular homogenisation area is 0.3m, contains, on average, eight particles and the best-fit displacement gradient tensor is obtained for each particle. Since the averaging region is a small proportion of the model dimensions, contours of (maximum shear) strain are typically quite irregular. We present both finite and incremental strain contours to illustrate fault evolution. Incremental strains are calculated in 1cm throw intervals, where for each particle the accumulated

displacement of the previous stage is subtracted. The best-fit deformation tensor for each 1cm throw increment can then be obtained for each particle using the same method described above.

For the definition of the stress and strain paths at selected locations within our model (Fig. 8) we use 1m diameter homogenisation areas, containing on average 92 particles, to minimize noise. Strain paths are represented using Mohr circles for the deformation tensor, which are briefly reviewed in Appendix A.

3 Results

3.1 *Macroproperties of model material*

Stress vs. axial strain (Fig. 4a and b) and volumetric strain (strictly speaking area change in a 2D model) vs. axial strain (Fig. 4c and d) curves for the strong and weak model material are shown in Fig. 4 (high resolution models, 5m wide and 10m high). Additionally maximum shear strain contour plots for selected biaxial test samples are shown (Fig. 4e and f) in order to illustrate strain localisation. The strong material exhibits elasticity and compaction prior to failure (Fig. 4a). The axial strain at failure and the differential stress at failure increase with increasing confining pressure (Fig. 4a). The amount of strain softening decreases with increasing confining pressure, i.e. the material becomes more ductile. The weak material exhibits steady-state flow after a non-linear increase in differential stress (Fig. 4b). The steady-state stress increases with increasing confining pressure. The lack of strain softening in the weak material is probably due to the use of rigid platens as lateral boundaries, which do not allow the formation of a single through-going shear zone (O'Sullivan pers. comm., 2004). A comparison of the volumetric strain curves for the strong and weak material (Figs. 4c and d) reveals that at low confining pressures (e.g. 25MPa, see also max. shear strain

229 contour plots, Figs. 4e and f) the weak material dilates and localises earlier than the
230 strong material. However, from these figures it is clear that the strong material
231 localises strain better because it exhibits greater strain softening.
232 Young's modulus and Poisson's ratio (assuming plane strain, Potyondy and
233 Cundall, 2004) were obtained for the unconfined biaxial tests (sample width 1m, N =
234 30) and determined at half the axial strain to failure and are 21.8 ± 1.6GPa and 0.29 ±
235 0.06, respectively. Principal stress diagrams with best-fit failure envelopes are shown
236 in Fig. 5. For the strong material a Coulomb-Mohr criterion with tension cut-off (Paul,
237 1961) was fitted using the results of direct tension tests on dog-bone shaped samples.
238 The best-fit parameters with curves representing probabilities that data points lie on
239 the left hand side of the failure envelope are plotted in Fig. 5 and reveal that the
240 unconfined compressive strength, cohesion and friction coefficient are typical of those
241 for strong sedimentary rocks (e.g. Hoek and Brown, 1997; Tsiambaos and
242 Sabatakakis, 2004). However, the ratio of unconfined compressive strength to tensile
243 strength is low (3.5) compared to natural rocks (e.g. 9 –17, table 6.15.1 in Jaeger and
244 Cook, 1976). These low ratios are typical for DEM models using smooth, circular
245 particles (Fakhimi, 2004) and can be improved using either irregular shaped particles
246 (clumps), by introducing a bending resistance between chains of bonded particles
247 (Cundall pers. comm., 2004) or by increasing sample resolution (table 3 in Potyondy
248 and Cundall, 2004). For the purpose of this article in which we examine fault
249 localisation within a brittle/ductile sequence, absolute strength values are subordinate
250 with strength contrast and rheology the main controlling factors. For the non-bonded
251 material the average friction coefficient was calculated from the confined biaxial tests
252 as 0.47 ± 0.05 (standard deviation). The Coulomb-Mohr criterion is plotted using the
253 average friction coefficient and no cohesion (Fig. 5).

In summary, material properties and rheology of the strong layers are comparable with those of strong sedimentary rocks (e.g. Hoek and Brown, 1997; Tsiambaos and Sabatakakis, 2004), whilst the weak layers have no tensile strength and are comparable to some shales (e.g. Petley, 1999).

3.2 *Fault growth and geometry in a multilayer sequence*

Figure 6 shows the propagation of a fault through a multilayer model at throw (*t*) increments of 1cm. The stages of fault evolution are illustrated with contours of incremental maximum shear strain for each stage. Although the total 10cm offset is not visible from the layer interfaces, fault development can be examined from the changing pattern of low incremental strains. Figure 6 is complemented by the profiles of strain and rotation for layer E at 2cm throw increments (Fig.7), which were obtained using 1m wide circular homogenisation regions with a spacing of 10cm.

At low displacements (< 3cm) diffuse zones of deformation develop on either side of the lowest strong layer (G). Up to throws of 3cm, formation of a low-amplitude precursory fold within this strong layer is accommodated by flow in the underlying and overlying weak layers. At a throw of 4cm, the lowest strong layer (G) fails in tension (Mode I fracture) and subsequent strain is concentrated on this fault. At throws of 5cm to 7cm, flow in the weak layers accommodates folding of the second strong layer (E) until it fails in tension arising from outer-arc extension associated with monoclinal folding; folding is highlight by the rotational plateaux shown in Fig.7. Flow in the weak layers is principally accommodated within diffuse zones that are located in the hanging wall of the incipient fault and have an overall antithetic shear sense (see below). These antithetic shear zones intersect the tops of the strong layers at the point of greatest outer arc extension associated with

monoclinal folding. At a throw of 8cm two additional Mode I fractures have formed, one in the topmost layer (A), collinear with the array of underlying Mode I fractures, and another one in the hanging wall of the lowest layer (G). The latter is located on the hanging wall hinge of the monoclinal flexure of the lowermost strong layer and propagates from bottom to top, a direction that is again consistent with outer arc extension. At this stage one of the strong layers (C) is still intact, even though it is overlain and underlain by strong layers containing an approximately collinear array of Mode I fractures, demonstrating that the failure of layers within a multilayer does not necessarily occur in forward sequence. At a throw of 9cm the fault has cut through all of the strong layers within the sequence and although it begins to localise within the weak layers, it has yet to do so in the central weak layer. This anomaly arises due to the localisation of a second Mode I fracture in the second lowest strong layer (E). This new fracture formed in the hanging wall side of the earlier fracture, which became inactive over the 8 - 9cm interval but became active again between 9 - 10cm throw. At 10cm throw a continuous, through-going fault is established. This fault has a 'staircase' geometry, in which vertical faults within the strong layers are linked by approximately 50° dipping faults in the weak layers, producing an average dip of *ca* 60°. Although individual fault segments first develop within strong layers and do not progress simply from bottom to top of the model, the final geometry is relatively simple and coherent. This coherence suggests that the deformation of both strong and weak layers throughout the model is strongly coupled, details of which are investigated below.

3.3 *Stress and strain paths*

The centre diagram in Fig. 8 shows the model in Fig. 6 at the final throw of 10cm contoured for maximum finite shear strain (contour interval is 0.01). Strain and stress paths were determined at 12 selected locations (Fig. 8). In each circular region of 1m diameter the average stress tensor and displacement gradient tensor were obtained at 1cm throw intervals. For the strong layers, six locations of Mode I fracturing were analysed, four along the eventual through-going fault and two hanging wall splays. In the weak layers, four regions were examined between the main Mode I fractures in the strong layers and along the eventual through-going fault, and two regions were selected within the low-angle antithetic shear zones in the hanging wall of the eventual through-going fault. The strain paths are shown in Fig. 8 using Mohr circles for the deformation tensor (see Appendix A for a brief review). Rotations and stretches are easily read off these diagrams (see Fig. A-2 for ideal deformation paths) and large volumetric strains can be simply calculated by the product of the principal stretches. However, the volumetric strains and rotational components of strain in this model were initially small and are therefore shown separately in Fig. 9 for each locality. Stress paths are shown in principal stress diagrams in Fig. 10, in which the experimental derived failure envelopes for the strong and weak material (Fig. 5) are plotted.

The strain and stress paths of the 12 locations identified in Fig. 8 are described in four groups sharing similar evolutionary paths. Each of these groups represents a key kinematic element of the localisation of the fault within the modelled multilayer. For simplicity the groups are referred to in geometric terms relative to the eventual through-going fault and depending on whether they occur within strong or weak layers. They are each described in the general order in which they develop: (i)

antithetic shear zones - weak layers, (ii) synthetic faults, strong layers, (iii) synthetic faults – weak layers, (iv) hanging wall splays – strong layers; whilst the structures i and iv represent accommodation features associated with fault displacement, the synthetic faults (ii and iii) eventually become the through-going fault. Though the emphasis is on describing the basic deformation paths for each element, we also highlight the coupling and inter-relationships between them. The location of each locality is shown in Fig. 8 (with locality names ranging from A through to H according to the layer), and individual strain and stress paths for each of these locations are shown in Figs. 8, 9 and 10.

(i) Antithetic shear zones – weak layers:

The two locations (D2 and F2) straddling antithetic shear zones in weak layers show similar strain/stress paths, though the zone closer to the base of the model and the future main fault (F2) shows, as expected, the larger volumetric strain and finite strain. These zones are dilational (Fig. 9b) with generally counter-clockwise (CCW) shearing (positive rotation in Fig. 8 and 9d), a dominant pure shear component (Fig. 8) and link downwards into eventual Mode I fractures which form the main fault within the strong layers (Fig. 6). Their formation is evidently related to monoclinal folding of the intervening strong layers because they link the eventual Mode I fractures arising from outer arc folding of underlying strong layers with the complementary monoclinal hinge on the base of overlying strong layers (Fig. 7). After the first throw increment (1cm) the weak material at both locations is in its critical stress state (Fig. 10b) and thereafter shows an almost linear increase in volumetric strain with throw (Fig. 9b). The continued growth of these antithetic shears suggests that flexuring within the hanging wall of the eventual main fault continues beyond the formation of Mode I fractures within the strong layers (Fig. 7), a feature which is

ascribed to the irregularity of the trace of the eventual through-going main fault (see below). A temporary levelling off of volumetric strain at one location (D2, Fig. 9b) is attributed to the short-term cessation of extension across the Mode I fracture in the second lowest strong layer (location E1).

(ii) Synthetic faults – strong layers:

Four locations (A, C, E1 and G1; Fig. 8) straddle the trace of the main fault within the strong layers and show similar stress/strain paths, though timing differs from one location to another. Initially the deformation at each location is characterised by clockwise (CW) rotation (negative values in Fig. 9c) accompanied by approximately linear increase in volumetric strain (Fig. 9a) and progressive increase in σ_{I} and decrease in σ_{III} (Fig. 10a). These deformations are consistent with monoclinal folding prior to fault localisation (Fig. 7). Tensile failure, i.e. Mode I fracture, of each strong layer is marked by a rapid increase in the local volumetric strain (Fig. 9a), a slight increase in rate of rotation (Fig. 9c) and, generally, by a corresponding stress release (increase in σ_{III}, Fig. 10a). The rapid volumetric strain changes and associated Mode I fracture formation do not, however, migrate progressively up the model with time. From the base of the model Mode I fracturing starts in the strong layers at 3cm throw (G1), *ca* 4.5cm (E1), 8cm (C) and 7cm (A), respectively. After Mode I fracturing, most locations are characterised by simple extension (Fig. 8) with increasing dilational CW shear (Fig. 9a and c), arising from pull-apart formation. A temporary cessation of displacement on the second lowest layer (at E1) is marked by a gradual increase in CW rotation (Fig. 9c) and a decrease in both σ_{I} and σ_{III} (Fig. 10a), with approximately constant volumetric strain (Fig. 9a). This is due to the formation of a Mode I fracture in the hanging wall of the main fault, which is active in the last two throw increments shown (see hanging wall splay – strong layer, location E2).

(iii) Synthetic faults – weak layers:

Four locations (B, D1, F1 and H) straddle what is to become the main fault within the weak layers. One of these (location H) reaches an advanced stage very early because it is adjacent to the pre-defined fault and therefore attains high strains at low throws, immediately reaching the critical stress state of the weak material (Fig. 10b) and thereafter showing approximately linear increases in volumetric strain with throw (Fig. 9b). The rotational component at this location shows a dramatic increase after a throw of 4cm (Fig. 9d), which coincides with the formation of the first Mode I fracture (location G1). In contrast the other locations (B, D1 and F1) are characterised by early stage CW rotations (Fig. 9d) with variable degrees of compaction (Fig. 9b), which are usually accompanied by increases in σ_{I} and little change in σ_{III} (Fig. 10b). Later stage decreases in both σ_{I} and σ_{III} (Fig. 10b) together with increases in volumetric strain (Fig. 9b) are associated with dilational CW shearing with a dominant simple shear component (Fig. 8). Rotation associated with monoclinal flexure occurs in each weak layer from the onset but increases abruptly at a throw of 8cm (Fig. 9d) when the final strong layer (C) is broken and elevated shear strains occur along the entire fault trace (Fig. 6). This late stage deformation reflects fault linkage and the relative shallow dip of the linking faults within the weak layers. At this stage the weak material is in a critical stress state (Fig. 10b) and thereafter shows an approximately linear increase in volumetric strain with throw (Fig. 9b). Again the overstep generation is not progressive with linkages occurring at *ca* 4cm throw in the lower part of the model (at F1), at *ca* 8cm towards the top of the model (at B) and at *ca* 10cm towards the middle of the model (at D1). Though the deformation paths of each of the locations are similar, slight differences may offer some clues to the localisation process. The retarded localisation of a through-going fault at D1 is

402 associated with the relatively high compaction (-0.14%) accommodated during the
403 early stages of localisation at this location. It may also be that this retardation is, in
404 turn, responsible for the relatively late localisation in the overlying strong layer (C) as
405 well as the temporary cessation of movement on the underlying strong layer (E1).
406 Whether these links are causal is unclear, but they suggest that the behaviour at
407 different locations along the localising fault is strongly coupled.
408 (iv) Hanging wall splays – strong layers:
409 These two locations (E2 and G2) straddle what are to become hanging wall splays
410 within the strong layers. Although the faults dip towards the main fault, their sense of
411 shear is in sympathy with the main fault (Fig. 8 and 9c). The two locations show
412 similar strain paths, though again the precise timing of events at each is different.
413 Prior to Mode I failure at these locations (up to 7 - 8cm throw) small linear increases
414 in volumetric strain (up to 0.25%, Fig. 9a) are accompanied by substantial CW
415 rotations (*ca* 1º, Fig. 8 and 9c), rapid decreases in σ_{III}, and slight increases in σ_{I} (Fig.
416 10a). The significant rotations again record the development of precursory monoclines
417 within the strong layers, a feature which in outcrop studies would generally be
418 referred to as normal drag (e.g. Barnett, et al., 1987; Grasemann et al., 2005). When
419 throws of *ca* 3cm (at G2) and 6cm (at E2) are reached, Mode I fractures develop
420 within the same layers (at G1 and E1 respectively; Fig. 6), along the trend of the
421 incipient main fault, causing stress release and an increase in σ_{II} (Fig. 10a). Even
422 after Mode I failure varying degrees of rotation continue to occur at these locations
423 (Figs. 7 and 9c), a feature, which is attributed to the irregularity of the trace of the
424 newly formed through-going fault. In both cases stress paths are looped or bouncing
425 (Fig. 10a) indicating repeated failure of layers, before rapid increases in volumetric

strain (Fig. 9a) and stress release (increase in σ_{III}) correspond to the formation of Mode I fractures (after *ca* 7cm throw at G2, and 8cm throw at E2).

In the above discussion we consider only the local stress/strain response within the model. A proxy for the global stress/strain response of the strong layers can be obtained by tracing the strain energy stored in the bonds (i.e. elastic cement) and the bond breakage events. The average strain energy stored in each bond and the total number of broken bonds vs. throw are plotted in Fig. 11a. An initial non-linear increase in strain energy is followed by a slight drop in energy due to failure (and thus removal of bonds) of the lowest layer (G). This drop in energy is accompanied by a large increase in the number of broken bonds (Fig. 11a). After the first failure, both, the strain energy and number of broken bonds increase gradually until the next layer (E) fails. The failure of layer A and C show similar patterns. The drop in strain energy increases with increasing throw and no increase in strain energy is observed after the last strong layer failed (C) and a continuous fault has been established. Following localisation, the strain energy progressively decreases, stabilizing at a value equal to about half the peak value at a throw of 0.5m (not shown).

The stress/strain paths and the strain energy/number of broken bonds described above are consistent with conceptual models of fault growth in layered sequences. Fault growth can be summarised as a three-stage process (Fig. 11b):

1. Monoclinal flexure: Folding is accommodated in the strong layers by elastic bending prior to failure but by flow in the weak layers, which cannot sustain bending moments. Extension and folding leads to horizontal tensile stresses within the strong layers.
2. Failure of strong layers: Fault segments in the strong layers develop within the precursor monocline. The layers fail in tension and Mode I fractures

form. Failure of the strong layers leads to release of tensile stress (increase in σ_{III}) and a rapid increase in volumetric strain. After the first increment of failure, which is pure Mode I, the fractures develop a shear component due to the formation of pull-aparts within the strong layers. Despite the formation of fractures in the strong layers much of the offset is still accommodated by monoclinal folding to provide a zone of fault-related normal drag.

3. Formation of through-going fault: After failure of all strong layers a through-going fault develops with localisation of strain in the weak layers, at a throw of *ca* 0.1 m. Segment linkage leads to a staircase-geometry, with steeply dipping fault segments in the strong layers and relatively shallow dipping faults in the weak layers. With the formation of a through-going fault, normal drag becomes progressively less significant with increasing throw so that discontinuous shear displacement accounts for up to 60% and 85% of the total offset at throws of 0.5 and 1m, respectively.

It is important to emphasize that only one model is analysed in detail in this study. Different model realisations, with different particle and bond spatial distributions (but identical microproperty statistical distributions) exhibit variable fault geometries due to differences in the locations of stress concentrations causing fracture nucleation. Although the exact locations of fractures and the magnitude and sense of stepping across weak layers will vary between realisations, the overall fault dip and the relative timing and mode of failure (strong layers first as Mode I fractures) is not affected by varying particle and bond spatial distributions.

4 Implications for the 3D geometry of faults in multilayer sequences

The ideal conceptual image of a normal fault is that of a continuous surface entirely contained within a volume of rock and bounded by an elliptical tip-line (Watterson, 1986; Fig. 3b); more irregular tip-lines are attributed to the interaction with a free surface or other faults (Nicol et al., 1996). For the ideal fault, displacement varies continuously over the fault surface, with contours of displacement concentric about a central maximum. Relative to this simple model, our numerical model is best suited to modelling the displacement accumulation along a vertical chord from the maximum displacement to the upper tip line. For normal faults this chord is characterised only by displacement parallel propagation, with no out-of-plane or lateral propagation (Fig. 3b). Although our modelling demonstrates that, at least in its early stages, the localisation of individual faults is, perhaps not surprisingly, more complex than simple models suggest, the general upward progression of deformation away from the maximum displacement does adhere to that of the simple model. This suggestion is developed further by combining interpretations, using both finite (not shown) and incremental maximum shear strain contour diagrams (Fig. 6), of the cross-sections for different throw values of our DEM model, to produce a fence diagram of the fault traces. The fault tip-points on this fence diagram are joined to form continuous fault tip-lines outlining a series of fault segments (Fig. 12) which together represent a fault with a maximum displacement of 10cm at one end and zero displacement on the other. Because the 3D fault plane shown in Fig. 12 is based on 2D modelling, it does not take account of out-of-plane, or lateral, propagation effects, which are likely to increase the complexities associated with fault zone localisation. Nevertheless, the diagram illustrates several interesting features. Firstly, the degree of segmentation decreases with increasing displacement until the segmented array is eventually

replaced by a continuous fault. Secondly, despite the segmented nature of the fault, its overall shape approximates to one quadrant of an elliptical fault surface; the retarded localisation within layer C is responsible for the most significant departure from an approximately elliptical form. Thirdly, displacement transfer across contractional steps is possible even when segmented arrays are underlapping, i.e. the structure between beds E and G at a throw of 4 - 8cm. Finally, despite the complex nature of the fault on this scale of observation, the fault segments form a coherent array which, when considered together, resemble a simple single fault. In detail, of course, the segmented fault array shows a tip line that is more advanced in the strong layers (labelled A, C, E and G) than in the weak ones, a feature which suggests that within multilayer sequences tip-lines will, in detail, be fringed. It also shows that linkage of faults in layers C and E via a shallow dipping fault in the intervening weak layer produces a branch point where the segmented array gives way laterally to a continuous fault. Most of all, this geometry emphasizes the fact that the linkage of initially vertically segmented faults does not imply that the faults grew independently, a feature which is consistent with earlier models for segmented fault arrays (Childs et al. 1995, 1996; see also the coherent growth model of Walsh et al. 2003).

Our numerical models therefore provide a basis for extending the simple conceptual diagrams of Fig. 2 into 3D. Figure 13 shows that a continuous fault with nearly constant displacements in cross-sectional view can give way laterally to a fringed tip-line in which fault segments within strong layers are more advanced than those within weak layers. For simplicity the block diagram in Fig. 13 considers only segmentation arising from lateral propagation. In reality segmentation will be preserved over an entire fault surface if displacements are not high enough to link between strong layers. An increase in displacement, whether or not it is accompanied

by fault propagation, will lead to the progressive replacement of the segmented array by a continuous fault. Even where the fault is segmented we should expect displacements to vary systematically over the fault surface. However, when account is taken of both the discontinuous displacements on the fault and the continuous displacements accommodated by fault-related ductile deformations adjacent to the fault, displacement variations are reduced. In proportional terms, ductile deformation is likely to be more significant early in the localisation process, when fault segments remain unlinked. Continuity of displacement and related strains reflects the underlying fact that segments within an initially segmented array form a geometrically and kinematically coherent system, in which neither the displacements nor the locations of segments are incidental (coherent growth model, Walsh et al., 2003; see also Childs et al. 1995).

5 Discussion

The Discrete Element Method (DEM), as implemented in *PFC-2D,* has been used to model the growth of a normal fault in a brittle/ductile multilayer. The principal advantage of the DEM compared to continuum methods (Finite Element, Finite Difference and Boundary Element Methods) is that discrete fractures and faults with a large finite displacement can be more effectively modelled; advances in combined approaches (DEM-FEM) may, however, provide better means for future fault and fracture modelling. The main limitations in the modelling approach in this study are that the model materials are strain-rate independent and that fluids and their effects (e.g. over-pressuring, precipitation of minerals) are neglected. Despite these limitations, the modelling is capable of reproducing many of the characteristic features of natural faults, providing a mechanical rationale for their geometry and

549 growth. In particular, it provides a basis for investigating whether normal faults in
550 layered sequences localise first in the strong layers or the weak layers (Ferrill and
551 Morris, 2003), a question that cannot be addressed using conventional mechanical
552 analyses such as Mohr diagrams (Mandl, 2000).

553 The DEM models presented in this article incorporate properly calibrated
554 model materials that reproduce the behaviour of natural rocks. The brittle/ductile
555 multilayer sequence comprises strong layers, which are brittle at low to intermediate
556 confining pressures and have elastic properties and strengths similar to those of strong
557 sedimentary rocks, interbedded with weak layers, which are cohesionless, frictional-
558 plastic, and cannot sustain bending moments. Faulting in such a layered sequence
559 leads to an increase in layer parallel tensile stress (decrease in σ_{III}) and an increase in
560 volumetric strain in the strong layers until the material fails in tension (Mode I).
561 Diffuse zones of pure shear dominated deformation (squeeze flow) in the weak layers
562 accommodate small amplitude precursor folding of the strong layers prior to failure.
563 Deformation in these zones has a small rotational component which is antithetic with
564 respect to the main fault, and is in that respect similar to the antithetic 'damage zones'
565 at the tip of faults in homogeneous, non-layered rocks described by Kim et al. (2003).
566 Although both types of antithetic faults form within a zone of distributed shear, the
567 geometries of antithetic faults in our DEM models are strongly affected by layering,
568 in that they link the hinges of a fault related monocline. In our model Mode I fractures
569 within the strong layers form an initial vertically segmented fault array which is later
570 linked via shallow dipping faults in the weak layers. The model results provide a
571 mechanical basis for fault refraction arising from different modes of faulting within
572 different layers, with tensile failure in the strong layers and shear failure in the weak
573 layers. At overburden pressures greater than that applied here (> *ca* 100MPa) the

strong layers in this model fail in shear rather than in tension, but even in these circumstances faults tend to initiate first within the strong layers and the fault zone is an initially vertically segmented array. As in the low effective stress model the fault dips within the strong layers are controlled by the failure mode, whereas the fault dips within the weak layers are mainly controlled by segment linkage.

The model suggests also that abandoned fault tips or splays are not essential features of an initially vertically segmented array. Fault segments which underlap and do not generate abandoned tips and splays when they link, can form coherent arrays and show complementary displacement transfer, provided the intervening volume can accommodate ductile strains. The model highlights the fact that the initially vertically segmented fault array is geometrically and kinematically coherent (Walsh and Watterson, 1991; Walsh et al., 2003) and that the fault segments do not grow independently in individual layers (Benedicto et al., 2003) but could link laterally into a continuous fault (fig. 9 in Childs et al., 1996).

The model also demonstrates that initial Mode I fracturing is not necessarily an indicator of high pore pressure (as suggested for example by McGrath and Davison, 1995). Fluid pressure only increases the depth of possible tensile failure since it decreases the effective stress. Fault refraction at low effective stress is not ‘due to high pore pressure’ but due to different types of failure (extension vs. shear) in the different lithologies (Peacock and Sanderson, 1992). The suggestion that fault segmentation is a product of fault propagation (e.g. Jackson, 1987; Mandl, 1987; Cox and Scholz, 1988; Peacock and Zhang, 1993, Childs et al., 1996, Walsh et al., 2003, Marchal et al., 2003) is supported by DEM modelling, though the importance of mechanical layering in controlling segmentation cannot be overstated.

6 Conclusions

The Discrete Element Method (DEM), as implemented in *PFC-2D*, has been used for modelling the growth of a normal fault within a brittle/ductile multilayer sequence. Our research suggests that the DEM is capable of modelling the failure and localisation processes of faulting, aspects that cannot be modelled adequately using conventional continuum based methods. Our modelling provides new insights into both the mechanics and kinematics of faulting at low effective stresses and suggests the following principal conclusions:

- Large dip variations, and related fault refraction, are due to different types of failure (extension vs. shear) of layers.
- Normal faults in brittle/ductile sequences localise first in strong layers as steeply dipping Mode I fractures and are later linked via shallow dipping faults in weak layers.
- Faults contained in multilayer sequences have fringed tip lines, where the fault is laterally more advanced in the strong layers than in the weak layers. The extent of fringing is a function of strength contrast between the layers and fault displacement.
- Models for the 3D segmentation of faults in sedimentary sequences must include the effects of rock properties and mechanical layering.

Acknowledgement

Stimulating discussions with the other members of the Fault Analysis Group and the UCD Geophysics Group are gratefully acknowledged. Andy Nicol is acknowledged for fruitful discussion on many aspects of fault growth. Peter Cundall and Dave Potyondy (Itasca Consulting Group, Minneapolis) are thanked for their suggestions

624 and support regarding *PFC*. Catherine O'Sullivan is acknowledged for providing her
625 strain homogenisation codes, which helped in the development our own, and for
626 discussions regarding strain in discontinua. David Marsan clarified the use of the
627 least-square method for obtaining best-fit displacement gradient tensors. Schöpfer
628 thanks Win Means for a copy of his GSA Meeting (1992) workbook 'How to do
629 anything with Mohr circles (except fry an egg)', which clarified the use of Mohr
630 circles. Constructive reviews by Dave Sanderson and Jeffrey Loughran are gratefully
631 acknowledged. Schöpfer's PhD thesis project was funded by Enterprise Ireland (PhD
632 Project Code SC/00/041) and a Research Demonstratorship at University College
633 Dublin.

634

635 **Appendix A**

636 *Mohr Circles for* **D**

637 An extremely useful graphical representation of the position gradient tensor is the
638 Mohr circle for **D** (e.g. Means, 1983 and 1990).

639 Any two-dimensional, homogeneous deformation can be written as

640

641 $$\begin{pmatrix} x_1 \\ x_2 \end{pmatrix} = \begin{pmatrix} D_{11} & D_{12} \\ D_{21} & D_{22} \end{pmatrix} \begin{pmatrix} X_1 \\ X_2 \end{pmatrix} \qquad \text{(A-1a)}$$

642

643 or more compactly as

644

645 $$\mathbf{x} = \mathbf{DX}, \qquad \text{(A-1b)}$$

646

where **X** and **x** are position vectors for a particle in the undeformed and deformed state, respectively, and D_{11}, D_{12}, D_{21} and D_{22} are the components of the position gradient tensor **D**, which contains information about the stretch and rotation and is referred to as the deformation tensor in this Appendix.

The components of **D** can be obtained by deforming a unit square into a parallelogram (Fig. A-1a). Components D_{11} and D_{21} are determined using the x_1 and x_2 coordinates of the corner point that was located at (1,0) whereas components D_{12} and D_{22} are obtained using the x_1 and x_2 coordinates of the corner point that was located at (0,1) in the undeformed state.

A Mohr circle (of the first kind; De Paor and Means, 1984) representing **D** is drawn using equally calibrated axes for the normal (D_{11}, D_{22}) and shear components (D_{12}, D_{21}). Two points are plotted at (D_{11}, $-D_{21}$) and (D_{22}, D_{12}), connected by a line and a circle is drawn about this line (Fig. A-1b). The polar co-ordinates of any point on the **D** circle gives the stretch and rotation of a material line.

The principal stretches, s_I and s_{III} ($s_I > s_{III}$) can be graphically obtained by intercepting the circle with a line drawn from the origin through the centre of the circle (Fig. A-1b). The diameter of the Mohr circle is therefore related to the intensity of stretching, since the ellipticity of the strain ellipse is s_I/s_{III}. The volumetric strain (strictly speaking area change), which cannot be directly read off the Mohr diagram, is the product of the principal stretches minus one.

Symmetric deformation tensors ($D_{12} = D_{21}$) represent irrotational deformation and Mohr circles have their centre on the horizontal axis (Fig. A-2b and d). Mohr circles of this kind are often referred to as Mohr circles for stretch. Asymmetrical deformation tensors ($D_{12} \neq D_{21}$) represent rotational deformation (Figs. A-1, A-2a and c). The rotational component of any strain is given by

672

673 $$\tan\omega = \frac{D_{21} - D_{12}}{D_{11} + D_{22}} \qquad \text{(A-2)}$$

674

675 and can be obtained graphically by measuring the angle between a line drawn
676 from the origin to the centre of the circle and the horizontal axis, where by definition
677 clockwise rotation is negative (Fig. A-1b). Off-axis circles centred above the
678 horizontal axis represent deformation with a clockwise (by convention negative)
679 rotational component (Fig. A-2a and c).

680 Rigid body rotation leads to circles with zero radius and centres on a unit
681 circle in the Mohr diagram (Fig. A-2e). In this study it has proven useful to plot a unit
682 circle with its centre in the origin and lines with slopes in 1º intervals (Fig. 8). These
683 guidelines assist in estimating the amount of rigid body rotation prior to stretching.

684 The maximum angular shear strain is given by

685

686 $$\tan\psi_{\max} = \frac{s_I^2 - s_{III}^2}{2 s_I s_{III}} \qquad \text{(A-3)}$$

687

688 and can be obtained graphically by drawing a chord through the centre of the
689 circle perpendicular to the line that passes through the principal stretches (Fig. A-1b).
690 The intersection of the chord with the circles gives the points that represent material
691 lines that were perpendicular to each in other in the undeformed state (as usual double
692 angles are measured in Mohr circles). This pair of lines experienced the maximum
693 shear strain, since they are symmetrically arranged with angles of ±45º to the principal
694 stretches in the undeformed state (Fig. A-1b).

695

References

Barnett, J. A. M., Mortimer, J., Rippon, J. H., Walsh, J. J., Watterson, J. 1987. Displacement geometry in the volume containing a single normal fault. Bulletin of the American Association of Petroleum Geologists 71, 925-937.

Benedicto, A., Schultz, R. A., Soliva, R. 2003. Layer thickness and the shape of faults. Geophysical Research Letters 30, 2076, doi:10.1029/2003GL018237.

Burbidge, D. R., Braun, J. 2002. Numerical models of the evolution of accretionary wedges and fold-and-thrust belts using the distinct-element method. Geophysical Journal International 148, 542-561.

Childs, C., Watterson, J. & Walsh, J. J. 1995. Fault overlap zones within developing normal fault systems. Journal of the Geological Society London 152, 535-549.

Childs, C., Nicol, A., Walsh, J. J., Watterson, J. 1996. Growth of vertically segmented normal faults. Journal of Structural Geology 18, 1389-1397.

Cox, S. J. D., Scholz, C. H. 1988. On the formation and growth of faults: an experimental study. Journal of Structural Geology 10, 413-430.

Crider, J. G., Peacock, D. C. P. 2004. Initiation of brittle faults in the upper crust: a review of field observations. Journal of Structural Geology 26, 691-707.

Cundall, P. A., Hart, R. 1992. Numerical modeling of discontinua. Engineering Computations 9, 101-113.

Cundall, P. A., Strack, O. D. L. 1979. A discrete numerical model for granular assemblies. Géotechnique 29, 47-65.

De Paor, D. G., Means, W. D. 1984. Mohr circles of the First and Second Kind and their use to represent tensor operations. Journal of Structural Geology 6, 693-701.

721 Eisenstadt, G., De Paor, D. G. 1987. Alternative model of thrust-fault propagation.
722 Geology 15, 630-633.
723 Fakhimi, A. 2004. Application of slightly overlapped circular particles assembly in
724 numerical simulation of rocks with high friction angles. Engineering
725 Geology 74, 129-138.
726 Ferrill, D. A., Morris, A. P. 2003. Dilational normal faults. Journal of Structural
727 Geology 25, 183-196.
728 Finch, E., Hardy, S., Gawthrope, R. 2003. Discrete element modelling of
729 contractional fault propagation folding above rigid basement fault blocks.
730 Journal of Structural Geology 25, 515-528.
731 Finch, E., Hardy, S., Gawthrope, R. 2004. Discrete-element modelling of extensional
732 fault-propagation folding above rigid basement fault blocks. Basin Research
733 16, 489-506.
734 Grasemann, B., Martel, S., Passchier, C. 2005. Reverse and normal drag along a fault.
735 Journal of Structural Geology 27, 999-1010.
736 Hazzard, J. F., Young, R. P., Maxwell, S. C. 2000. Micromechanical modeling of
737 cracking and failure in brittle rocks. Journal of Geophysical Research 105,
738 16,683-16,697.
739 Hoek, E., Brown, E. T. 1997. Practical estimates of rock mass strength. International
740 Journal of Rock Mechanics & Mining Science 34, 1165-1186.
741 Imber, J., Tuckwell, G. W., Childs, C., Walsh, J. J., Manzocchi, T., Heath, A. E.,
742 Bonson, C.G., Strand, J. 2004. Three-dimensional distinct element modelling
743 of relay growth and breaching along normal faults. Journal of Structural
744 Geology 26, 1897-1911.

745 Itasca Consulting Group, 1999. Particle Flow Code in Two Dimensions, Minneapolis,
746 MN, USA.
747 Jackson, P. 1987. The corrugation and bifurcation of fault surfaces by cross-slip.
748 Journal of Structural Geology 9, 247-250.
749 Jaeger, J. C., Cook, N. G. W. 1976. Fundamentals of rock mechanics, 2nd edition.
750 Chapman & Hall, London.
751 Kim, Y.-S., Peacock, D. C. P. & Sanderson, D. J. 2003. Mesoscale strike-slip faults
752 and damage zones at Marsalforn, Gozo Island, Malta. Journal of Structural
753 Geology 25, 793-812.
754 Mandl, G. 1987. Discontinuous fault zones. Journal of Structural Geology 9, 105-110.
755 Mandl, G. 2000. Faulting in brittle rocks. Springer, Berlin Heidelberg New-York.
756 Marchal, D., Guiraud, M., Rives, T. 2003. Geometric and morphological evolution of
757 normal fault planes and traces from 2D to 4D data. Journal of Structural
758 Geology 25, 135-158.
759 McGrath, A. G., Davison, I. 1995. Damage zone geometry around fault tips. Journal
760 of Structural Geology 17, 1011-1024.
761 Means, W. D. 1983. Application of the Mohr-circle construction to problems of
762 inhomogeneous deformation. Journal of Structural Geology 5, 279-286.
763 Means, W. D. 1990. Kinematics, stress, deformation and material behavior. Journal of
764 Structural Geology 12, 953-971.
765 Nicol, A., Watterson, J., Walsh, J. J., Childs, C. 1996. The shapes, major axis
766 orientations and displacement patterns of fault surfaces. Journal of Structural
767 Geology 18, 235-248.

768 Oda, M., Iwashita, K. 2000. Study of couple stress and shear band development in
769 granular media based on numerical simulation analyses. International Journal
770 of Engineering Sciences 38, 1713-1740.
771 O'Sullivan, C., Bray, J. D., Li, S. 2003. A new approach for calculating strain for
772 particulate media. International Journal for Numerical and Analytical
773 Methods in Geomechanics 27, 859-877.
774 Paul, B. 1961. A modification of the Coulomb-Mohr theory of fracture. Journal of
775 Applied Mechanics 28, 259-268.
776 Peacock, D. C. P., Sanderson, D. J. 1992. Effects of layering and anisotropy on fault
777 geometry. Journal of the Geological Society London 149, 793-802.
778 Peacock, D. C. P., Zhang, X. 1993. Field examples and numerical modelling of
779 oversteps and bends along normal faults in cross-section. Tectonophysics
780 234, 147-167.
781 Petley, D. N. 1999. Failure envelopes of mudrocks at high confining pressures. In:
782 Aplin, A. C., Fleet, A. J., Macquaker, J. H. S. (Eds.), Muds and Mudstones.
783 Geological Society of London Special Publication 158, pp. 61-71.
784 Potyondy, D. O., Cundall, P. A. 2004. A bonded-particle model for rock. International
785 Journal of Rock Mechanics and Mining Sciences 41, 1329-1364.
786 Strayer, L. M., Suppe, J. 2002. Out-of-plane motion of a thrust sheet during along-
787 strike propagation of a thrust ramp: a distinct-element approach. Journal of
788 Structural Geology 24, 637-650.
789 Tsiambaos, G., Sabatakakis, N. 2004. Considerations on strength of intact
790 sedimentary rocks. Engineering Geology 72, 261-273.
791 Walsh, J. J., Watterson, J. 1991. Geometric and kinematic coherence and scale effects
792 in normal fault systems. In: Roberts, A. M., Yielding, G., Freeman, B.,

(Eds.), The geometry of normal faults. Geological Society of London Special Publication 56, pp. 193-203.

Walsh, J. J., Bailey, W. R., Childs, C., Nicol, A., Bonson, C. G. 2003. Formation of segmented normal faults: a 3-D perspective. Journal of Structural Geology 25, 1251-1262.

Watterson, J. 1986. Fault dimensions, displacements and growth. Pure and Applied Geophysics 124, 365-373.

Figure captions

Figure 1: A small-scale normal fault (displacement = 30cm; downthrows to the right) exposed in a cliff-section east of Kimmeridge Bay, Dorset, UK, which illustrates the importance of lithological control on fault dip and fault refraction. This normal fault cuts a shale-dominated sequence (Kimmeridge Clay Formation, Upper Jurassic) that contains calcareous shale layers. Within these calcareous shales fault segments are nearly vertical and are linked via shallow dipping faults within the weaker shale layers. Fault displacement on this 'staircase' geometry leads to the development of pull-aparts.

Figure 2: (**a**) Schematic geometry of normal faults cutting limestone layers of the Cretaceous Buda Limestone exposed along Interstate Highway 10 (I-10), in west Texas and three possible models for their growth (**b**, **c** and **d**; after Ferril and Morris, 2003; table 1 and fig. 5). In (**b**) the faults localise first in the strong layers and the steep segments are later linked via shallow faults. In (**c**) the faults localise first in the weak layers and the shallow segments become linked via steep faults. In (**d**) the fault trace is not initially segmented but the trajectory of the upward propagating fault tip changes as it crosses a lithological interface, i.e. a bedding plane.

Figure 3: Model boundary conditions. (**a**) *PFC-2D* model consisting of >23,400 cylindrical particles. The strong and weak layers consist of bonded and non-bonded particles, respectively (bonds are shown in enlarged figure). Confining pressure is approximately 23MPa and the hanging wall moves with constant velocity parallel to a predefined fault at the base of the model. (**b**) Schematic block diagram showing the

826 propagation directions of an ideal elliptical normal fault. The tip line bounds an
827 elliptical area of failed rock (white). Since the fault plane propagates radially (arrows
828 show tip line propagation direction) only two sections (shaded) have no out-of-plane
829 fault propagation. The 2D numerical model is located within the plane of no lateral
830 fault propagation. This fault is shown schematically as a single fault surface, but in all
831 probability will comprise an array of segments.
832
833 **Figure 4:** (**a** to **d**) Plots illustrating the results of rheological testing of the strong (**a**
834 and **c**) and weak (**b** and **d**) materials comprising the multilayer models at various
835 confining pressures (labelled curves). Vertical dashed lines in are drawn at 0.3, 0.4
836 and 0.5% axial strain. (**e** and **f**) Contour plots showing the distribution of maximum
837 finite shear strain (contour interval is 0.005) within models comprising the strong (**e**)
838 and weak (**f**) materials at axial strains of 0.3, 0.4 and 0.5% and a confining pressure of
839 25MPa.
840
841 **Figure 5:** Principal stress diagram with best-fit failure envelopes (bold lines) for the
842 strong and weak material. The data for the strong material were obtained from direct
843 tension tests on dog-bone shaped samples with a central width of 1m at various
844 confining pressures and each data point represents the state of stress at failure (N =
845 196). The data for the weak material were obtained from confined (25MPa) biaxial
846 compression tests and each data point represents the peak stress during loading (N =
847 30). The best-fit macroproperties are given, where σ_{uc} = unconfined compressive
848 strength (MPa), T = tensile strength (MPa), C_0 = cohesion (MPa) and μ = friction
849 coefficient. For the strong material the different curves represent the 0.01, 0.5, 0.25,
850 0.50, 0.75, 0.95 and 0.99 percentile of the probability distribution. For the weak

material the average friction coefficient and the average ± 1 and ± 2 standard deviations are shown.

Figure 6: Incremental maximum shear strain contour plots (contour interval is 0.005) of a *PFC-2D* model of normal fault growth in a brittle/ductile sequence (*t* = throw). The different layers within the model are labelled A to H. See text for further explanation.

Figure 7: Strain profiles in 2cm throw increments (labelled in **b**) along the centre of layer E. The maximum finite shear strain (**a**) and the rotational component of deformation (**b**) were obtained for 1m wide circular homogenisation regions with 10cm spacing. The two vertical dashed lines are the locations of Mode I fractures (labelled E1 and E2; see Figs. 6 and 8). The plateaux of the curves in (**b**) correspond to the limb of the monocline, the left hand hinge of which fails at between 5cm and 6cm throw.

Figure 8: Strain paths at selected locations (circled regions labelled A - H) in the multilayer model. The central diagram is of the multilayer model at a finite throw of 10cm which is contoured for maximum finite shear strain (contour interval is 0.01). Individual beds within the multilayer are labelled A to H. Mohr circles for finite strain at 1cm throw increments are illustrated; arrows connect centres of successive Mohr circles. The dashed vertical arc in each Mohr diagram is part of a unit circle with its centre located at the origin. The centres of Mohr circles for rigid body rotation plot on this arc. The dash-dot lines are lines intersecting the origin with slopes in 1º intervals (labelled in B). These guidelines can give quick insights into rotations (e.g. 1º CW

rigid body rotation prior to formation of pull-apart as in diagram G2). See text and Appendix A for further explanation.

Figure 9: Graphs of volumetric strain (**a** and **b**) and the rotational component of deformation (**c** and **d**) vs. throw for the locations labelled in Fig. 8.

Figure 10: Principal stress paths for the locations labelled in Fig. 8 with experimentally derived failure envelopes (Fig. 5). Each arrow corresponds to the change of stress in a 1cm throw increment and dots represent the state of stress prior to faulting.

Figure 11: Three-stage development of fault growth in a multilayer sequence as illustrated by (**a**) plot of number of broken bonds and average strain energy per bond vs. throw recorded in the model shown in Fig. 6 and (**b**) schematic representation of stages in development of the same model. The data in (**a**) were obtained from the model by tracking each bond breakage event and the strain energy stored in the bonds. The onset of failure of each strong layer is labelled and marked with vertical dashed lines. In (**b**) monoclinal flexuring is exaggerated and only localised deformation is shown. The precursor zone of faulting (bounded by the two dashed lines) is idealised as a planar feature, whereas the modelled zone broadens upwards due to the predefined nature of the fault at the base of the model and free surface effects.

Figure 12: 3D fault plane constructed from interpreted fault traces from the *PFC-2D* model shown in Fig. 6 assuming the temporal fault zone evolution is equivalent to spatial variation in fault zone structure with increasing displacement. Labelled layers

(A, C, E and G) are strong layers. To construct this diagram, the lateral displacement gradient was taken as 1:150, i.e. 1.5m distance along strike between successive sections in Fig. 6. The fault is typically more advanced in the strong layers; the advancement within layer C is approximated, since no section is available at a throw of 8.5cm.

Figure 13: Conceptual growth model for normal faults cutting limestone layers of the Buda Limestone (see Fig. 2). The block diagram is located at a lateral fault tip (Fig. 3b). For simplicity the fault is shown with no vertical displacement gradient. The block diagram was constructed using cross sections shown in Fig. 2a and b.

Figure A-1: Plotting and reading Mohr circles for **D**. (**a**) The components of the deformation tensor (D_{11} etc.) are derived from the corners of the deformed unit square as shown. The deformation tensor for this parallelogram is also given. (**b**) Mohr circle representation of the **D** tensor. The constructions for finding the principal stretches, s_{I} and s_{III}, the rotational component of deformation, ω, and the maximum angular shear strain, $\psi_{\max}$, are illustrated. See Appendix A for further explanation.

Figure A-2: Illustrations of Mohr circles for deformation, **D**, for a range of strain paths. For each labelled example the Mohr circles and the corresponding deformed unit square in Cartesian coordinates (dotted lines) are shown (the finite state of strain is shown as solid lines and intermediate stages are shown as dashed lines). Strain paths in (**a**), (**b**) and (**c**) are constant volume deformation. The strain path shown in (**d**) is irrotational simple extension (dilation), (**e**) is rigid body rotation without stretching. and (**f**) is rigid body rotation (e.g. normal drag in the context of faulting) followed by

simple extension (e.g. the formation of a Mode I fracture). In (**d**) and (**f**) only one set of parallel lines exists that shows neither finite nor incremental stretch.

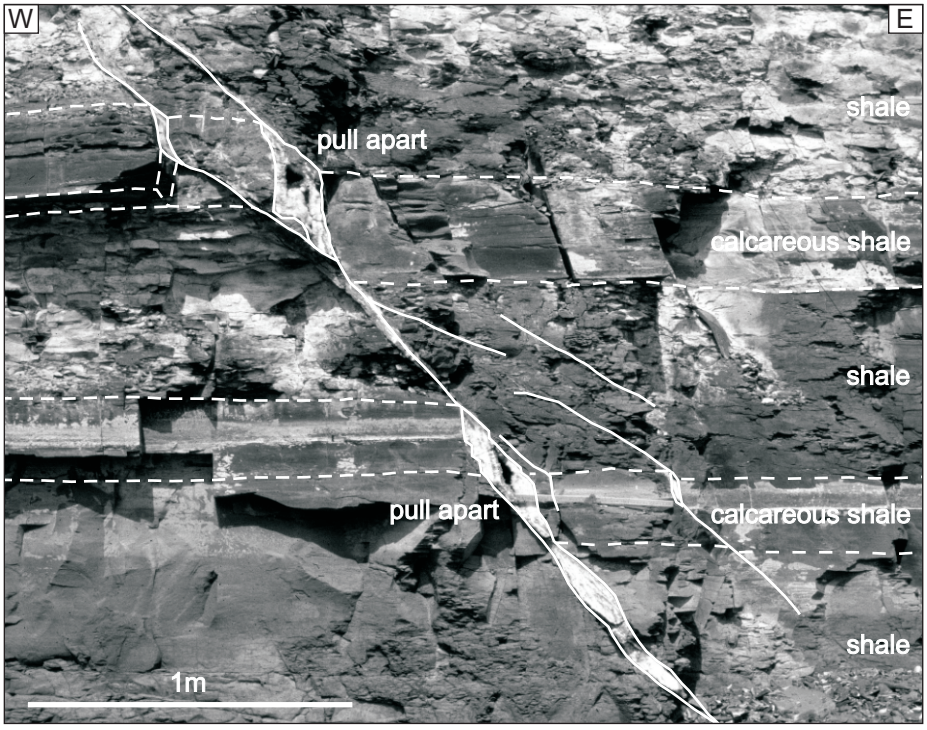
W
E
shale
pull apart
calcareous shale
shale
pull apart
calcareous shale
shale
1m

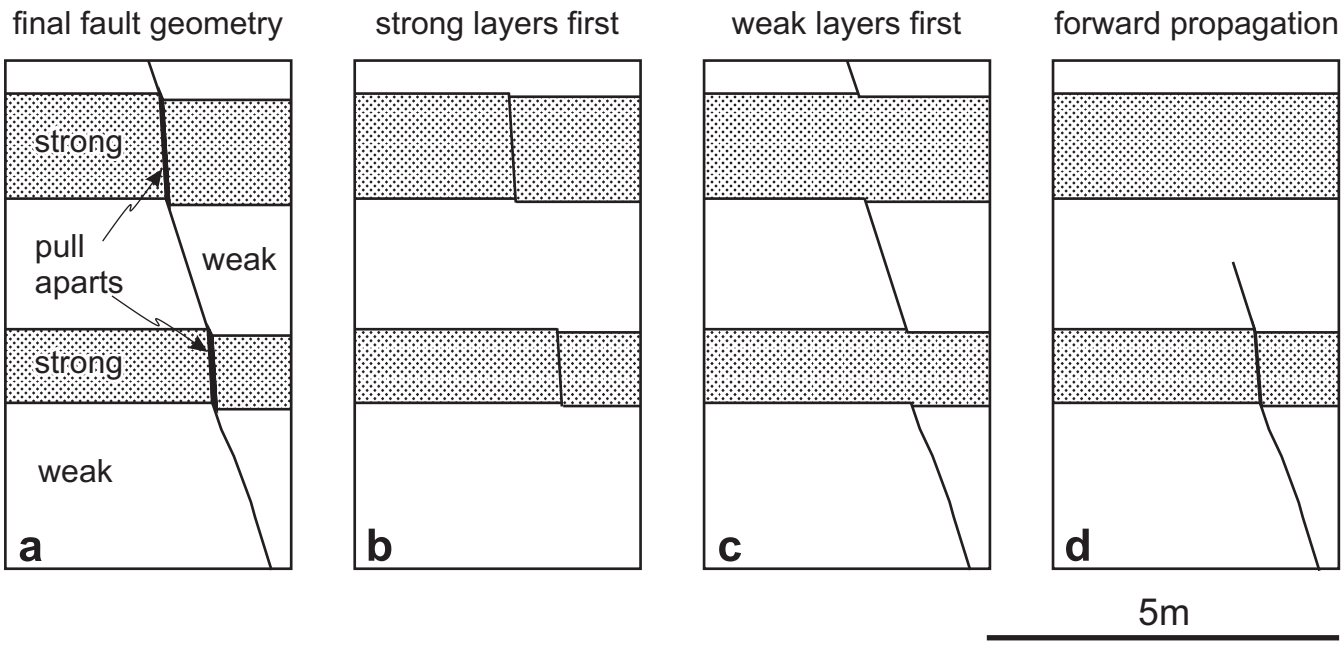
final fault geometry
strong layers first
weak layers first
forward propagation
strong
pull
aparts
weak
strong
weak
a
b
c
d
5m

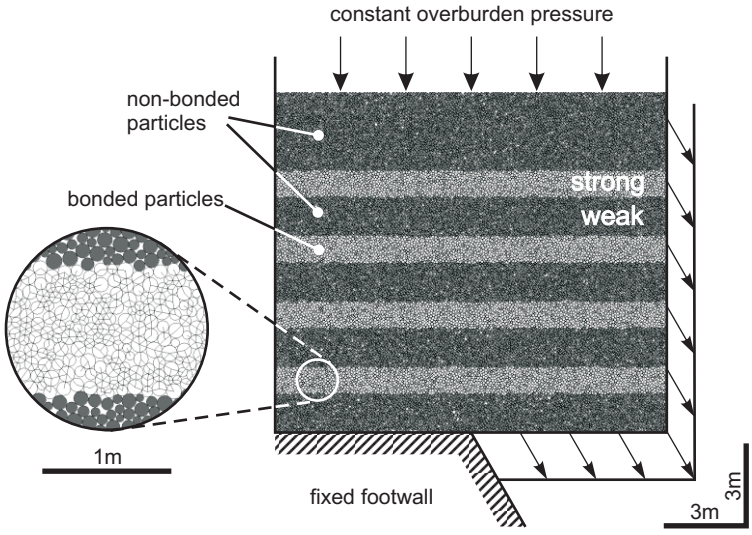
constant overburden pressure
non-bonded particles
bonded particles
strong
weak
1m
fixed footwall
3m
3m

(a)

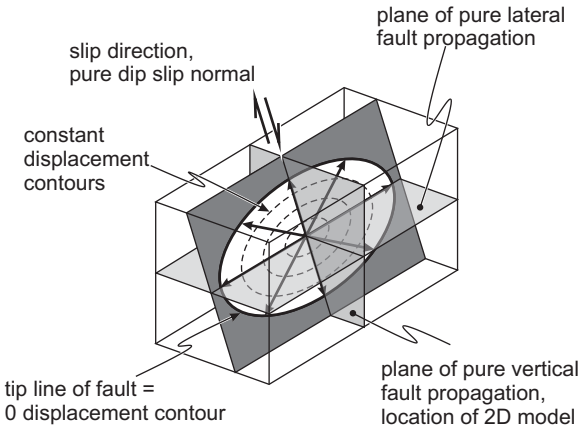
plane of pure lateral fault propagation
slip direction, pure dip slip normal
constant displacement contours
tip line of fault = 0 displacement contour
plane of pure vertical fault propagation, location of 2D model

(b)

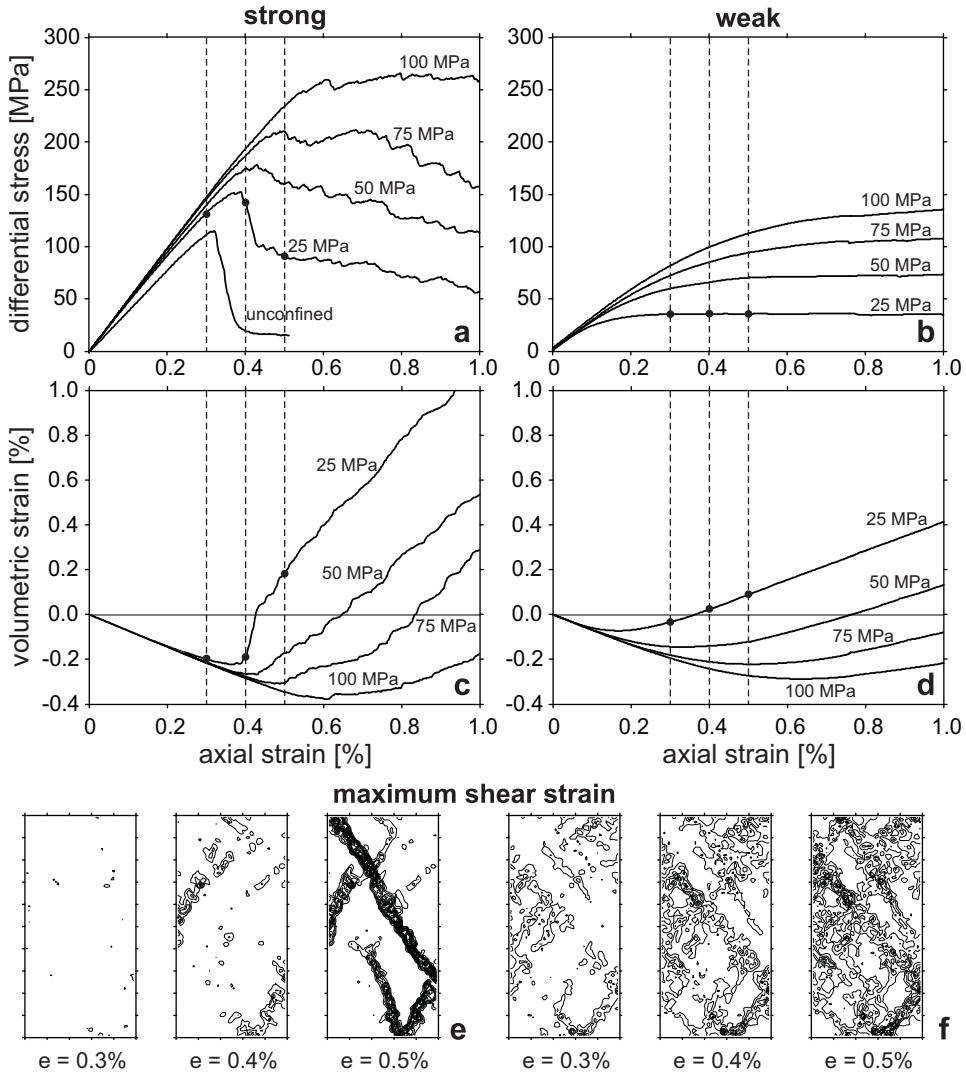
strong
weak
differential stress [MPa]
100 MPa
75 MPa
50 MPa
25 MPa
unconfined
a
b
volumetric strain [%]
c
d
axial strain [%]
axial strain [%]
maximum shear strain
e
f
e = 0.3%
e = 0.4%
e = 0.5%
e = 0.3%
e = 0.4%
e = 0.5%

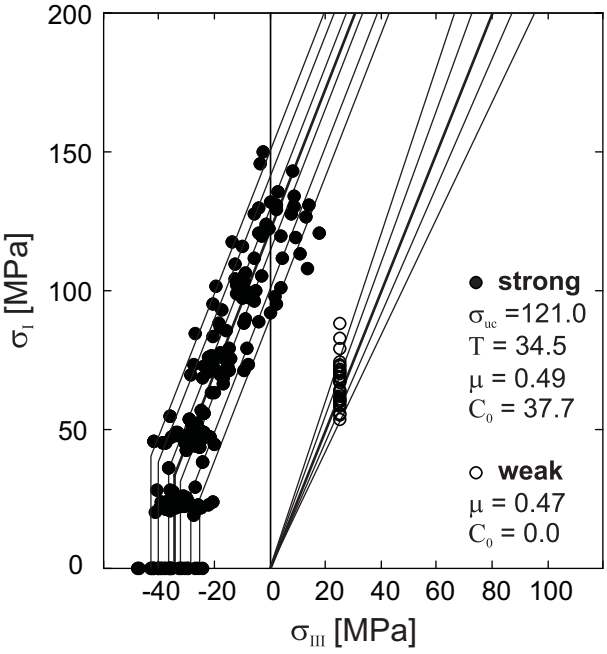
200
150
100
50
0
-40
-20
0
20
40
60
80
100
σI [MPa]
σIII [MPa]
strong
σuc =121.0
T = 34.5
μ = 0.49
C0 = 37.7
weak
μ = 0.47
C0 = 0.0

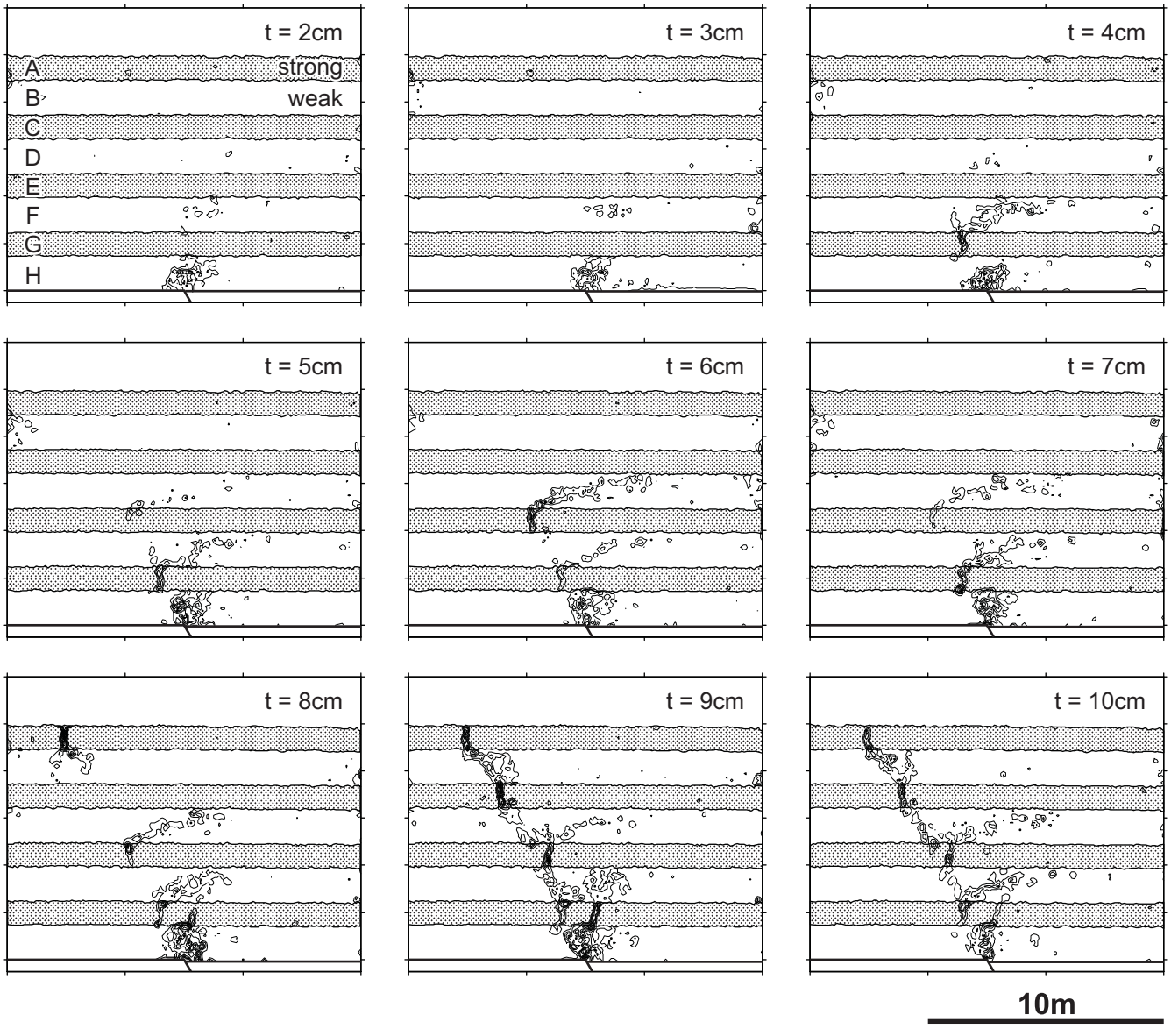
t = 2cm
A
strong
B
weak
C
D
E
F
G
H
t = 3cm
t = 4cm
t = 5cm
t = 6cm
t = 7cm
t = 8cm
t = 9cm
t = 10cm
10m

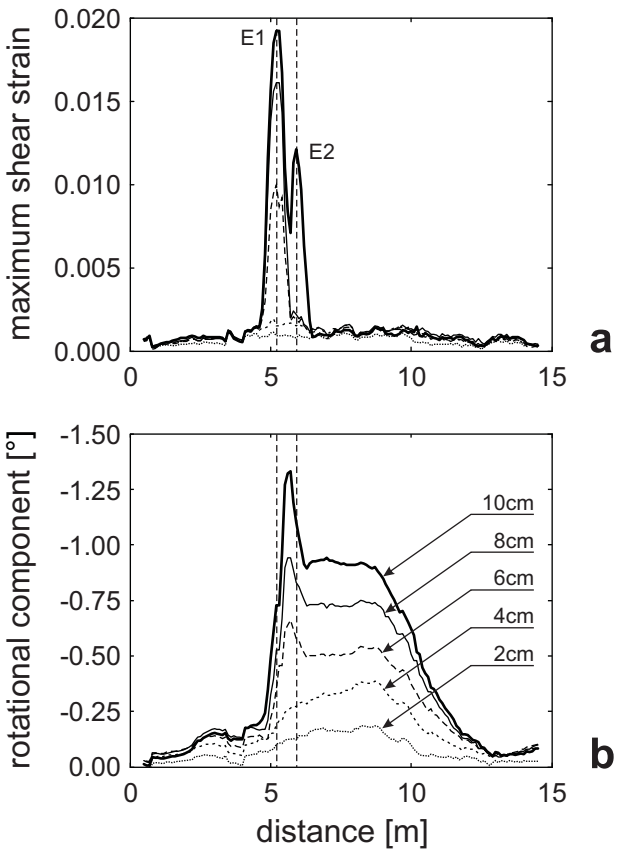
maximum shear strain
0.020
0.015
0.010
0.005
0.000
E1
E2
0
5
10
15
a
rotational component [°]
-1.50
-1.25
-1.00
-0.75
-0.50
-0.25
0.00
10cm
8cm
6cm
4cm
2cm
0
5
10
15
distance [m]
b

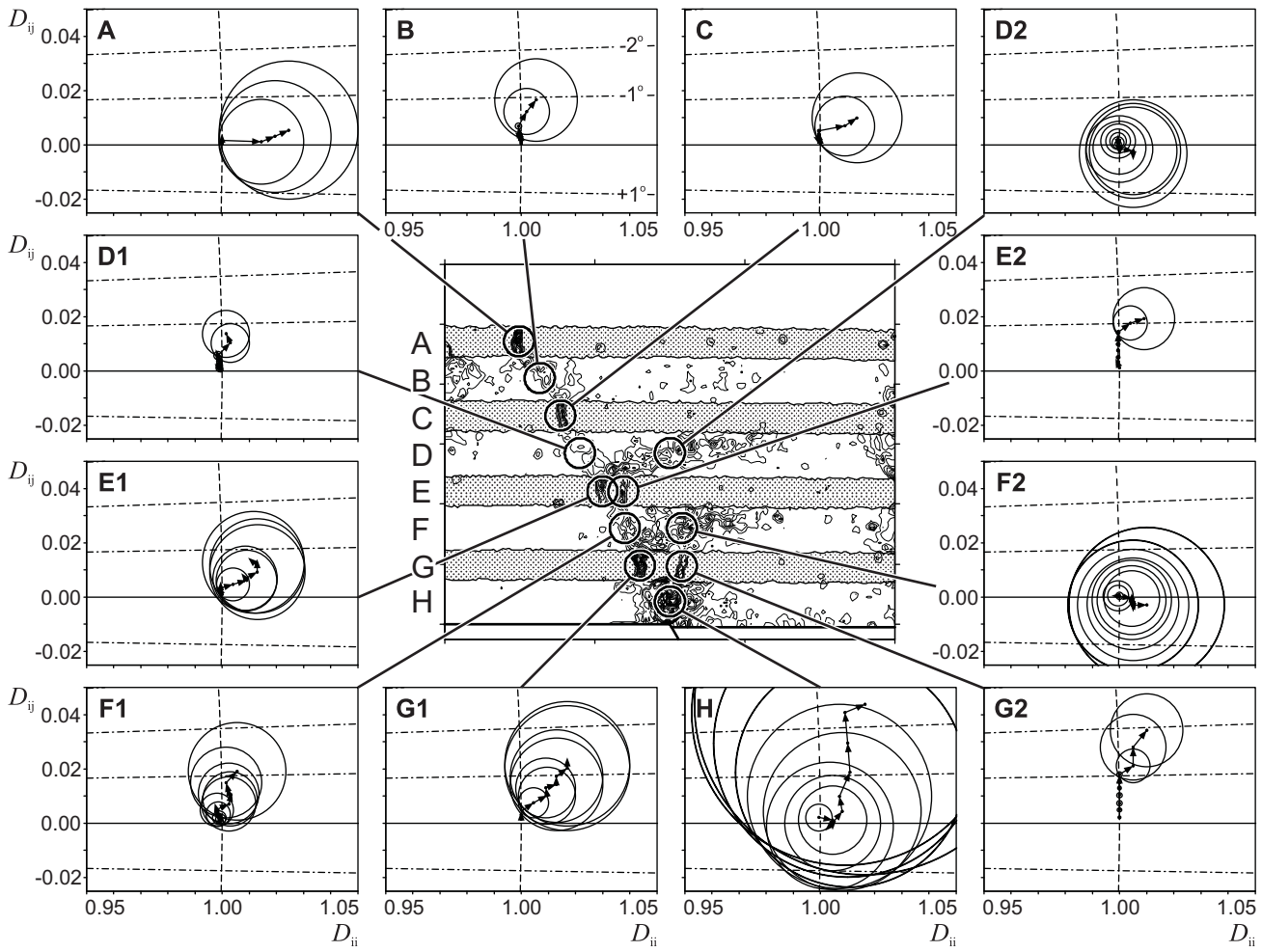
A
B
C
D1
D2
E1
E2
F1
F2
G1
G2
H
-2°
-1°
+1°
D_{ij}
D_{ii}
0.04
0.02
0.00
-0.02
0.95
1.00
1.05

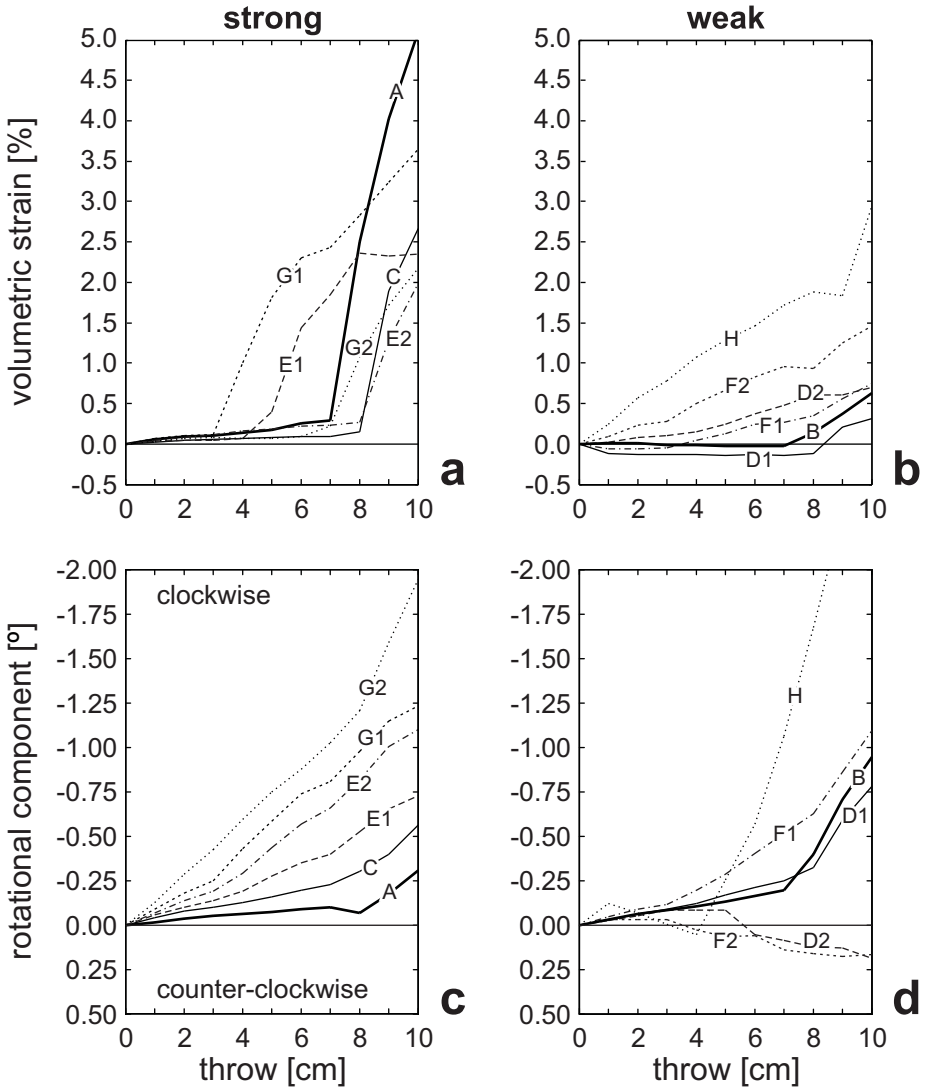
strong
weak
volumetric strain [%]
rotational component [°]
throw [cm]
clockwise
counter-clockwise
A
G1
C
G2
E2
E1
H
F2
D2
F1
B
D1
a
b
c
d

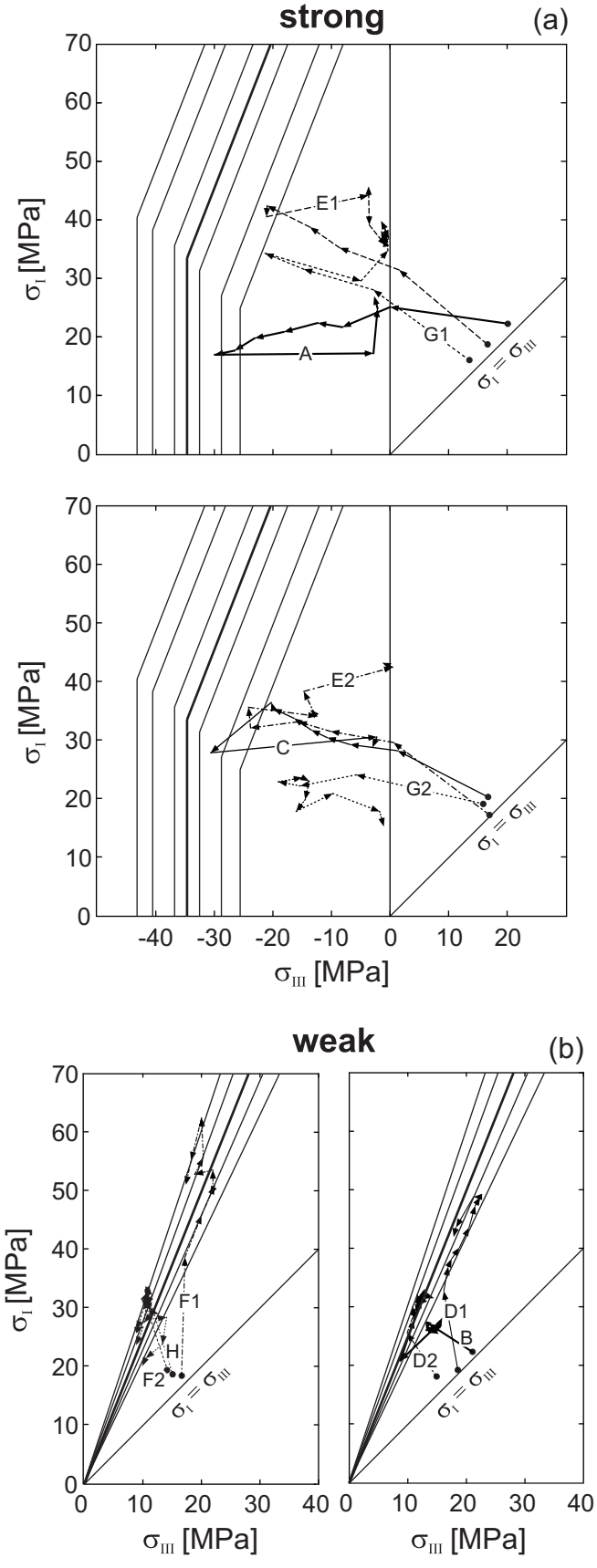
strong
(a)
σI [MPa]
E1
G1
A
σI = σIII
E2
C
G2
σIII [MPa]
weak
(b)
F1
H
F2
D1
B
D2

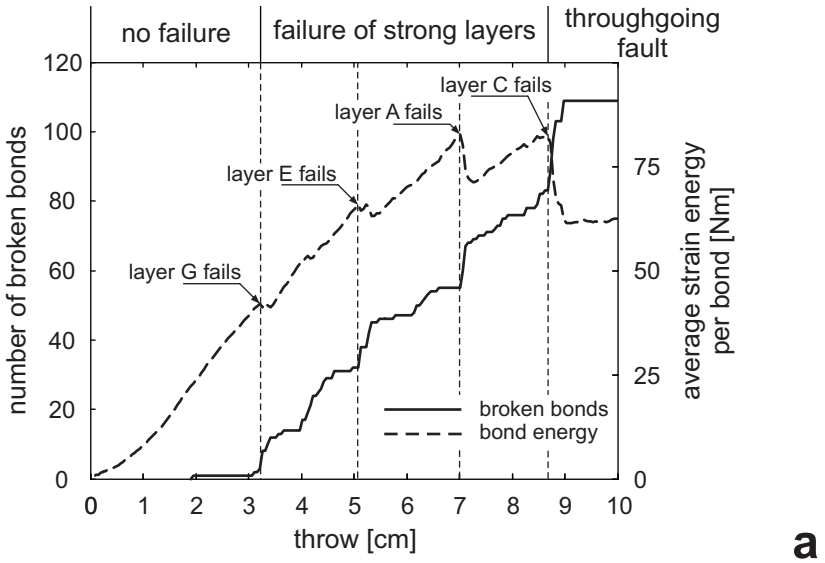
no failure
failure of strong layers
throughgoing fault
layer C fails
layer A fails
layer E fails
layer G fails
broken bonds
bond energy
number of broken bonds
average strain energy per bond [Nm]
throw [cm]
0
20
40
60
80
100
120
25
50
75
0 1 2 3 4 5 6 7 8 9 10

a

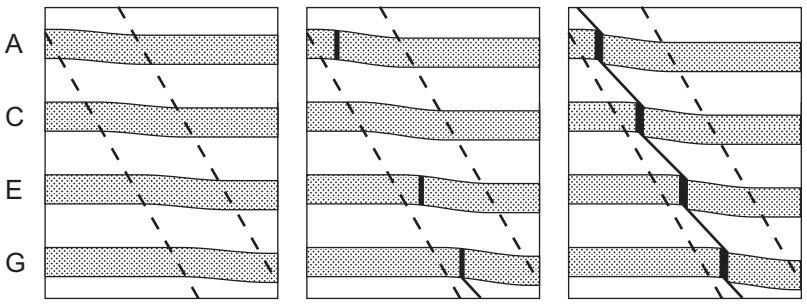
A
C
E
G

b

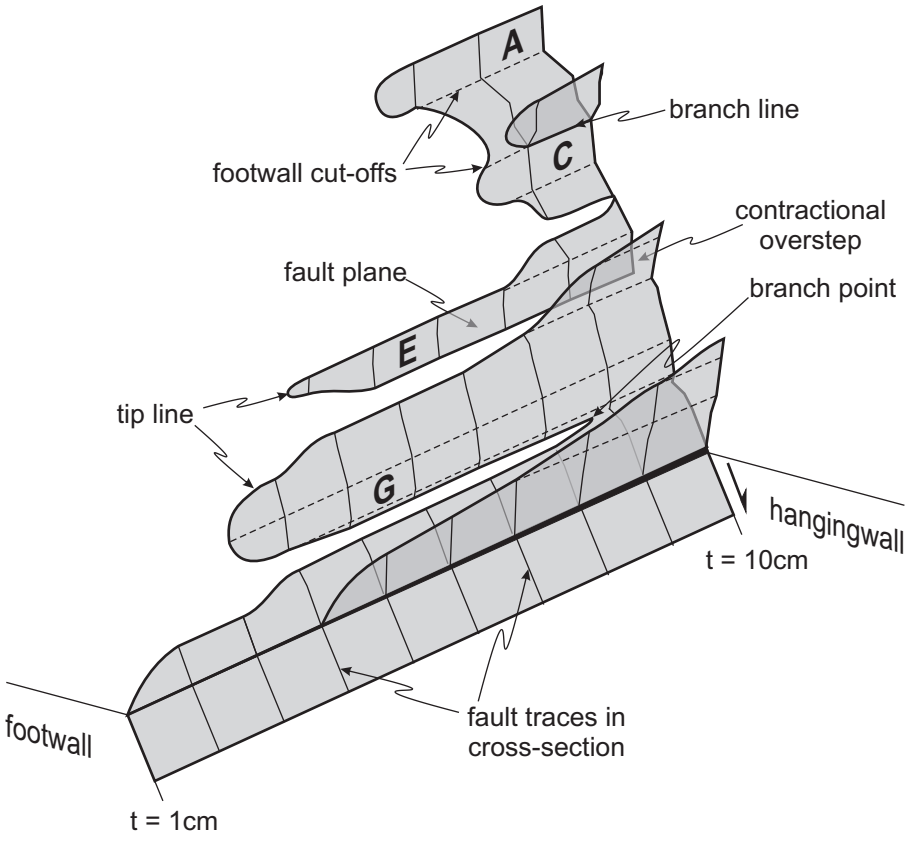
A
C
E
G
branch line
footwall cut-offs
contractional
overstep
fault plane
branch point
tip line
hangingwall
t = 10cm
footwall
fault traces in
cross-section
t = 1cm

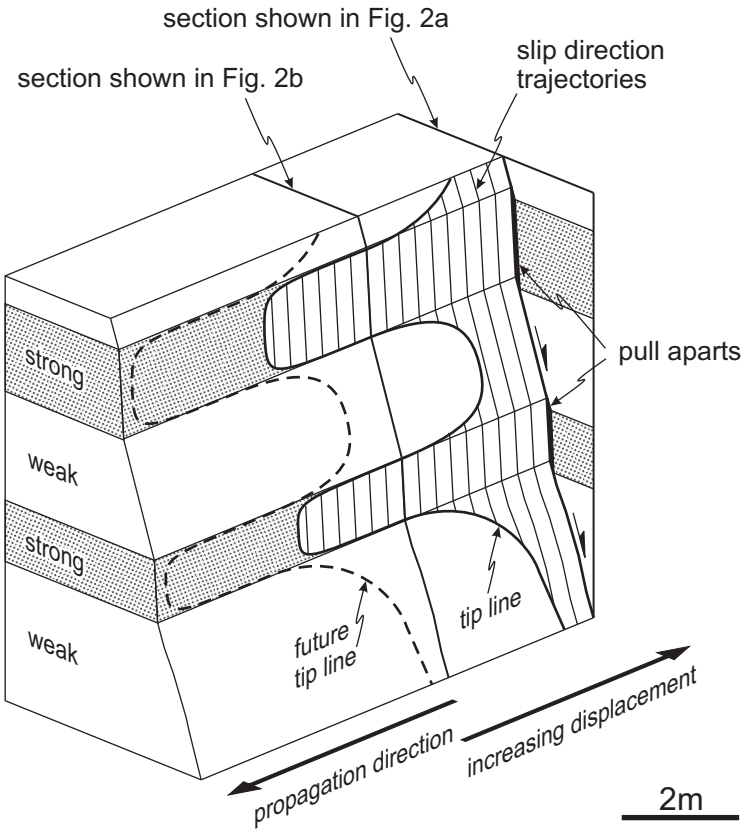
section shown in Fig. 2a
section shown in Fig. 2b
slip direction trajectories
pull aparts
strong
weak
strong
weak
future tip line
tip line
propagation direction
increasing displacement
2m

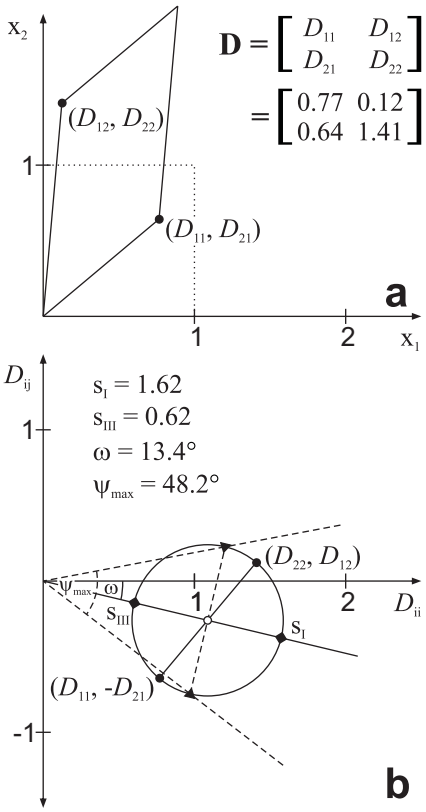
x2
D = [D11 D12 ; D21 D22]
= [0.77 0.12 ; 0.64 1.41]
(D12, D22)
1
(D11, D21)
a
1
2
x1
Dij
1
sI = 1.62
sIII = 0.62
ω = 13.4°
ψmax = 48.2°
(D22, D12)
ψmax
ω
1
2
Dii
sIII
sI
(D11, -D21)
-1
b

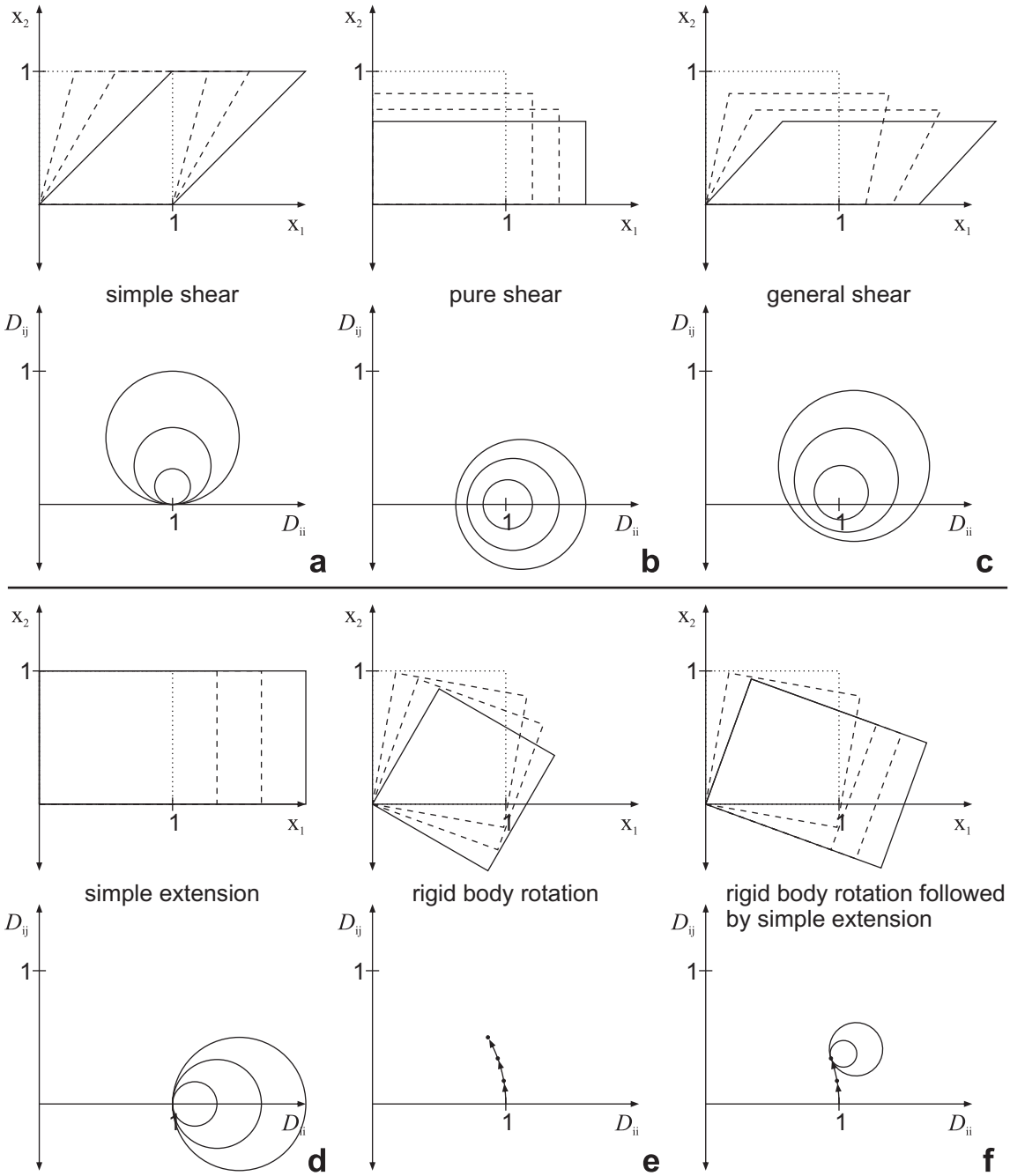
x2
1
1
x1
simple shear
pure shear
general shear
Dij
Dii
a
b
c
simple extension
rigid body rotation
rigid body rotation followed
by simple extension
d
e
f